Check for updates

ADVANCED FUNCTIONAL MATERIALS

www.afm-journal.de

Synthesis of CeO_x-Decorated Pd/C Catalysts by Controlled Surface Reactions for Hydrogen Oxidation in Anion Exchange Membrane Fuel Cells

Ramesh K. Singh, Elena S. Davydova, John Douglin, Andres O. Godoy, Haiyan Tan, Marco Bellini, Bryan J. Allen, Jasna Jankovic, Hamish A. Miller, Ana C. Alba-Rubio, and Dario R. Dekel**

Due to the sluggish kinetics of the hydrogen oxidation reaction (HOR) in alkaline electrolytes, the development of more efficient HOR catalysts is essential for the next generation of anion-exchange membrane fuel cells (AEMFCs). In this work, CeO_x is selectively deposited onto carbon-supported Pd nanoparticles by controlled surface reactions, aiming to enhance the homogenous distribution of CeO_x and its preferential attachment to Pd nanoparticles, to achieve highly active CeO_x-Pd/C catalysts. The catalysts are characterized by inductively coupled plasma–atomic emission spectroscopy, X-ray diffraction, high-resolution transmission electron microscopy, scanning transmission electron microscopy (STEM), electron energy loss spectroscopy, and X-ray photoelectron spectroscopy to confirm the bulk composition, phases present, morphology, elemental mapping, local oxidation, and surface chemical states, respectively. The intimate contact between Pd and CeO_x is shown through high-resolution STEM maps. The oxophilic nature of CeO_x and its effect on Pd are probed by CO stripping. The interfacial contact area between CeO_x and Pd nanoparticles is calculated for the first time and correlated to the electrochemical performance of the CeO_x-Pd/C catalysts. Highest recorded HOR specific exchange current (51.5 mA $mg^{-1}{}_{Pd}$) and H_2–O_2 AEMFC performance (peak power density of 1,169 mW cm^{-2} $mg_{Pd}{}^{-1}$) are obtained with a CeO_x-Pd/C catalyst with $Ce_{0.38}$/Pd bulk atomic ratio.

1. Introduction

Significant progress has been achieved recently in the field of anion exchange membrane fuel cells (AEMFCs).[1–3] In spite of the remarkable development of this technology, the deployment of AEMFCs is still hindered by the chemical degradation of the anion exchange membrane (AEM) and ionomers,[4–11] carbonation issues,[12–15] and by the sluggish kinetics of the hydrogen oxidation reaction (HOR).[2,16,17] It has been shown that the HOR kinetics in alkaline media is two to three orders of magnitude lower than that in acidic media,[18,19] even for the most active catalysts such as Pt,[17,19–22] Rh,[23] and Ir.[23] There are increasing efforts in the development of HOR electrocatalysts based on more abundant elements,[24–31] as well as Pd.[32,33] In order to increase the HOR kinetics of Pd, previous studies focused their efforts in the development of Pd-CeO_2 composites, as the most promising Pt-free catalyst for HOR.[34–39] The

Dr. R. K. Singh, Dr. E. S. Davydova, J. Douglin, Prof. D. R. Dekel
The Wolfson Department of Chemical Engineering
Technion - Israel Institute of Technology
Haifa 3200003, Israel
E-mail: dario@technion.ac.il

Dr. R. K. Singh, Prof. D. R. Dekel
The Nancy & Stephen Grand Technion Energy Program (GTEP)
Technion - Israel Institute of Technology
Haifa 3200003, Israel

The ORCID identification number(s) for the author(s) of this article can be found under https://doi.org/10.1002/adfm.202002087.

DOI: 10.1002/adfm.202002087

A. O. Godoy, Prof. J. Jankovic
Center for Clean Energy Engineering
University of Connecticut
Storrs, CT 06269, USA

Dr. H. Tan
UConn-ThermoFisher Scientific Center for Advanced Microscopy and Materials Analysis (CAMMA)
University of Connecticut
Storrs, CT 06269, USA

Dr. M. Bellini, Dr. H. A. Miller
Istituto di Chimica dei Composti Organometallici (CNR-ICCOM)
via Madonna del Piano 10, Sesto Fiorentino, Firenze 50019, Italy

B. J. Allen, Prof. A. C. Alba-Rubio
Department of Chemical Engineering
The University of Toledo
2801 W. Bancroft St., Toledo, OH 43606, USA
E-mail: ana.albarubio@utoledo.edu

use of ceria (CeO_2) is justified because i) it is an oxygen-deficient compound with a fast OH^- saturation[34,40] and ii) it has a high oxophilic character.[41]

The metal-metal oxide interaction on Pd-CeO_2 systems has been thoroughly investigated for several chemical reactions, such as CO oxidation, CH_4 oxidation, and NO reduction.[42–46] These studies focused on the formation of $Pd_xCe_{1-x}O_{2-\delta}$ local solid solutions, which provide tight contact and specificity on Pd-ceria based systems in catalysis. These have been thoroughly investigated by using extended X-ray absorption fine structure (EXAFS), X-ray photoelectron spectroscopy (XPS), Raman spectroscopy, and density functional theory (DFT) calculations.[42–46] Pd-CeO_2 systems have not only been studied in electrochemical but have also been widely used in environmental catalysis.[47–53] For example, Tan et al. investigated the support morphology-dependent catalytic activity of Pd/CeO_2 to eliminate indoor formaldehyde pollution.[47]

Several methods have been employed to prepare Pd/C-CeO_2 catalysts as an efficient HOR catalyst. Using a conventional chemical wet method, Miller et al. replaced 50% of the carbon catalyst support with CeO_2, followed by the deposition of Pd nanoparticles. The thus obtained Pd/C-CeO_2 catalyst exhibited a 20-fold improvement in the HOR activity compared to that of Pd/C in rotating disk electrode (RDE) measurements.[34] After careful analysis of the morphology of the catalyst, the authors claimed that the Pd particles are accumulated in the proximity of CeO_2, which helps in supplying OH_{ad} from CeO_2 to Pd-H_{ad}. The superior HOR activity of Pd/C-CeO_2 is hence attributed to the OH^- spillover from CeO_2 to Pd, which enhances the rate-limiting Volmer reaction alongside with weakening of the Pd-H bonding, and thus, the hydrogen binding energy (HBE)[34] (one of the descriptors of HOR activity[19,54,55]). This mechanism is also known as the bifunctional mechanism.[20,22,56] The decrease in HBE by the addition of CeO_2 to Pd was posteriorly demonstrated by DFT calculations.[37] In another work of the authors, the Pd metal loading was optimized in the Pd/C-CeO_2 catalysts, showing the best HOR activity for the case of 10 wt% Pd.[35]

More recently, Pd-CeO_2 catalysts have been prepared by using a spray flame-based process.[36] Using this method, the authors claim to increase the Pd-CeO_2 interface and with that, to enhance the catalyst performance. The reported HOR activity of this spray flame-prepared Pd-CeO_2 catalyst was further improved with respect to those previously reported. The highest HOR activity was observed when Pd nanoparticles are in intimate contact with CeO_2.[36] In another recent work, Yarmiayev et al. reported enhanced HOR activity of Pd through CeO_2 surface doping.[39] Based on the electrochemical surface area estimation, the authors claimed that the improved activity is due to a vertical growth of CeO_2 islands onto the Pd surface that enhances the Pd-CeO_2 interface area. The HOR activity with the highest CeO_2-doped material was improved by 50–100 times as compared to the pristine Pd and was mainly attributed to the change in HBE and the oxophilicity of CeO_2.[39] Ralbag et al. reported a novel method for entrapping CeO_2 onto a Pd lattice to obtained CeO_2@Pd with enhanced HOR activity.[38] The crucial role of the entrapped CeO_2 in improving the HOR catalytic activity was further explained by decreased HBE estimated from cyclic voltammograms. Although all these studies discuss the critical importance of increasing the interfacial area between Pd and CeO_2 particles, no quantitative measurement has yet been carried out.

In this work, a method based on controlled surface reactions (CSR) is used to synthesize a new type of CeO_x-Pd/C catalysts. This method has been reported in the literature for the selective deposition of metal or metal oxide onto metal nanoparticles, which ensures good interaction between the different components of the catalytic material.[57–61] We aim to obtain novel composite catalytic materials with ultra-high homogeneity of CeO_x distribution on the surface of carbon-supported Pd nanoparticles and a high interfacial area between Pd and CeO_x, which could not be obtained with previously reported methods. Quantitative estimation of the Pd and CeO_x contact area is also carried out in this study. This interfacial area measurement is highly useful in shedding light on the quality of the contact between the nanoparticles, affecting, in turn, the OH^- spillover from the CeO_x to the Pd nanoparticles. The CeO_x content in the composites is varied using sequential CSR cycles and was used to demonstrate the crucial role of the amount of CeO_x in the promotion of the HOR kinetics of the CeO_x-Pd/C catalysts. A comprehensive set of experimental techniques is used to follow the structural, morphological, and compositional changes occurring in the catalysts along with the CeO_x content variation, as well as to observe the evolution of the local and surface chemical state and the modification of the electrochemical properties of the CeO_x-Pd/C catalysts. Finally, a CeO_x-Pd/C catalyst prepared by the CSR method, selected with the highest activity towards HOR, is successfully tested in operando H_2–O_2 AEMFCs, showing its potential as HOR catalyst for this technology.

2. Results and Discussion

The bulk and surface compositions of the CeO_x-Pd/C catalysts were determined by ICP-AES and XPS, respectively, and are given in **Table 1**. As can be seen, CeO_x-Pd/C catalysts with a

Table 1. Bulk and surface compositions of Pd/C and CSR-synthesized CeO_x-Pd/C catalysts from ICP-AES and XPS measurements.

Catalyst	ICP-AES Pd bulk [wt%]	ICP-AES Ce bulk [wt%]	Calculated bulk Ce/Pd [at. ratio]*	ICP-AES Measured bulk Ce/Pd [at. ratio]	XPS Measured surface Ce/Pd [at. ratio]
Pd/C	9.08	0.00	0.00	0.00	0.00
0.24 CeO_x-Pd/C	7.67	2.47	0.26	0.24	0.42
0.38 CeO_x-Pd/C	7.87	3.99	0.39	0.38	0.66
0.59 CeO_x-Pd/C	7.82	6.06	0.65	0.59	1.56

* Based on Pd and Ce theoretical loadings (Section S1, Supporting Information).

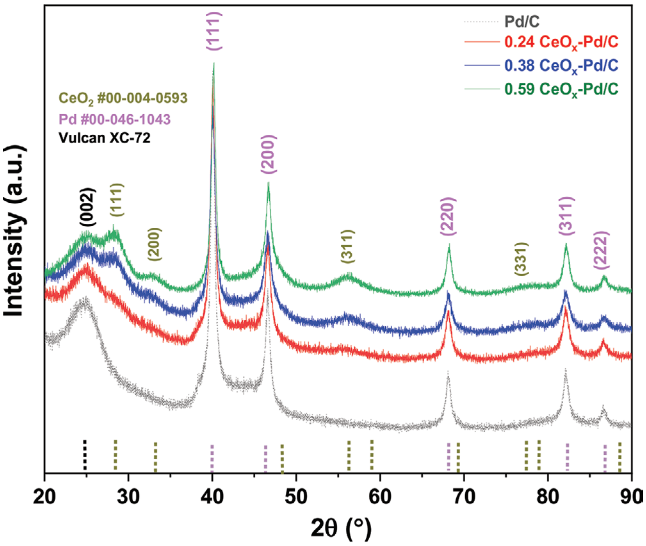

Figure 1. XRD patterns of Pd/C and CSR-synthesized CeO_x-Pd/C catalysts.

wide Ce/Pd atomic ratio range (0–0.65) have been successfully prepared by the CSR method. The Ce/Pd bulk atomic ratios measured after CSR cycles are similar to the calculated ratios based on the target composition (see the Supporting Information for more details), with a slight deviation for the catalyst with the highest loading. This suggests the saturation of the surface by CeO_x after several CSR cycles. If there is no available surface for the Ce precursor to bond, the precursor might get physically absorbed on the surface and easily decompose during the reduction step. The surface Ce/Pd atomic ratios are higher than those on the bulk, which is in agreement with the surface affinity of the CSR approach, in which the ceria nanoislands are deposited on the surface of the metal nanoparticles.[59–61] Based on the bulk composition obtained from ICP-AES measurements, the samples were labeled as n CeO_x-Pd/C, where n indicates the measured Ce/Pd bulk atomic ratio (0.24 CeO_x-Pd/C, 0.38 CeO_x-Pd/C, and 0.59 CeO_x-Pd/C).

The XRD patterns of monometallic Pd/C and the CSR-synthesized CeO_x-Pd/C catalysts are shown in **Figure 1**. Phases of Pd, CeO_2, and carbon are observed. The details of the reflections from each phase are given in the Supporting Information. With the addition of CeO_x, the intensity of the (111), (200), and (311) facets of CeO_2 (at 28.6°, 33.1°, and 56.3°, respectively) increases gradually. No shift is observed in the position of the XRD peaks for Pd after the incorporation of CeO_x, indicating that alloying is not taking place between Pd and CeO_x. Thus, any changes in the properties of the catalyst could be ascribed solely to the decoration of the Pd surface by CeO_x, rather than the bulk electronic effect. The details of the crystallite size calculation of CeO_2 are given in the Supporting Information. Unlike the Pd/C-CeO_2 composites reported earlier,[34] the CSR method results in the formation of low crystalline ceria nanoparticles, with crystallite size between 1.7–3.2 nm (see Table S1 in the Supporting Information), showing low-intensity XRD reflections with significant broadening.

Pd3d (Figure S1a–c, Supporting Information) and Ce3d (Figure S2a–c, Supporting Information) XPS spectra were recorded to get information about the chemical environment of Pd, CeO_x and their surface atomic composition. The Pd3d XPS spectrum of Pd/C is shown in Figure S3 in the Supporting Information. The Pd3d spectrum splits into two peaks corresponding to $3d_{5/2}$ and $3d_{3/2}$ due to the spin-orbit coupling. Each pair is fitted into three different Pd species of metallic Pd(0), Pd(II) and Pd(IV). The peak pair at lower binding energy is assigned to Pd(0) and those with higher binding energies to Pd(II) and Pd(IV), respectively. The metallic Pd(0) peak position is comparable to that reported in the literature.[36,62] The summary of the XPS spectra of the catalysts is given in **Table 2**. As seen in Table 2, the shift of 0.25 eV in the binding energy of Pd(IV) in the $Pd3d_{3/2}$ peak position might be due to the bimetallic interaction between Pd and CeO_x in the 0.38 CeO_x-Pd/C compared to Pd/C.[63] The concentration of Pd(IV) increases when increasing the Ce/Pd bulk atomic ratio until 0.38, and it decreases afterward. It is worth mentioning that the shift in the XPS peak to the lower binding energies of 0.59 CeO_x-Pd/C is highest (among nCeO_x-Pd/C) in comparison to Pd. This is mainly due to significantly higher CeO_x content at surface, which may lead to decreased availability of surface Pd (see the discussion on the electrochemical surface area in the later section). The Pd(IV)/Pd(0) ratio is 0.30, 0.36, 0.75, and 0.43 for Pd/C, 0.24 CeO_x-Pd/C, 0.38 CeO_x-Pd/C, and 0.59 CeO_x-Pd/C, respectively. Thus, the highest Pd(IV)/Pd(0) ratio

Table 2. Surface compositions and peak positions of Pd(0), Pd(II), and Pd (IV) species of Pd/C and CSR-synthesized CeO_x-Pd/C catalysts.

Catalyst	Pd species	Percentage	Pd $3d_{5/2}$ position [eV]	Pd $3d_{3/2}$ position [eV]	FWHM [eV]	
					$Pd_{5/2}$	$Pd_{3/2}$
Pd/C	Pd(0)	61.43	335.18	340.44	0.97	0.97
	Pd(II)	20.05	336.10	341.36	0.97	0.97
	Pd(IV)	18.52	337.65	342.91	2.20	2.20
0.24 CeO_x-Pd/C	Pd(0)	57.57	335.07	340.33	0.86	0.86
	Pd(II)	21.65	335.94	341.20	0.86	0.86
	Pd(IV)	20.78	337.40	342.66	2.20	2.20
0.38 CeO_x-Pd/C	Pd(0)	49.39	335.17	340.43	0.87	0.87
	Pd(II)	13.72	336.01	341.27	087	0.87
	Pd(IV)	36.89	337.40	342.66	2.20	2.20
0.59 CeO_x-Pd/C	Pd(0)	47.27	334.87	340.13	0.87	0.87
	Pd(II)	32.48	335.52	340.78	1.10	1.10
	Pd(IV)	20.25	337.16	342.42	2.20	2.20

Table 3. Ce 3d deconvolution results for the determination of %Ce(III) and %Ce(IV) of CSR-synthesized CeO_x-Pd/C.

Catalyst	Ce(III)/Ce(IV) area ratio	[%] Ce(III)	[%] Ce(IV)
0.24 CeO_x-Pd/C	0.26	20.6	79.4
0.38 CeO_x-Pd/C	0.23	19.0	81.0
0.59 CeO_x-Pd/C	0.21	17.2	82.8

present in 0.38 CeO_x-Pd/C results from partial charge transfer from metallic Pd to CeO_x. This observation is in line with previously reported results,[36] where the higher ratio of Pd(0)/Pd(II) arises from poor Pd and CeO_x homogeneity, as CeO_x contributes to lower reducibility of Pd. The lower percentage of metallic Pd in Pd/C, compared to 70% and 65% reported by Yu et al.[36] and Singh et al.[62], respectively, can be correlated with the smaller particle size. Typically, smaller particles are more oxidized than large particles as they have a larger fraction exposed to the environment.

Ce3d photoelectron spectra were also recorded to get information about the surface oxidation state of Ce (Figure S2a–c, Supporting Information). Deconvolution results suggest that the concentration of Ce(IV) species increases with the addition of CeO_x. The Ce(III)/Ce(IV) ratio was calculated from the Ce $3d_{5/2}$ signals, being 0.26, 0.23, and 0.21 for 0.24 CeO_x-Pd/C, 0.38 CeO_x-Pd/C, and 0.59 CeO_x-Pd/C, respectively (**Table 3**). According to Deshpande et al., there is a clear correlation between the concentration of Ce^{3+} sites and the CeO_x particle size, being the large particles richer in Ce^{4+}.[64] Therefore, our results indicate the formation of larger islands upon the addition of CeO_x. The amount of Ce(III) decreases when increasing the Ce/Pd ratio. In the case of 0.59 CeO_x-Pd/C, the high Ce/Pd surface atomic ratio (1.56 by XPS) contributes to a reduced proportion of Pd entering the CeO_x lattice.[65] This would explain the decreased concentration of Pd(IV) species in 0.59 CeO_x-Pd/C.

High-resolution transmission electron microscopy (HRTEM) images (**Figure 2**a–d) and the corresponding scanning transmission electron microscopy/energy-dispersive X-ray spectroscopy (STEM/EDS) maps (Figure 2e–h) of Pd/C and CSR-synthesized CeO_x-Pd/C catalysts are shown in Figure 2. As can be seen, Pd nanoparticles are uniformly distributed on the carbon support. Some minor agglomeration can also be seen, likely due to the sintering of the nanoparticles during the thermal treatments. Particle sizes of ≈3–4 nm were obtained for Pd/C and CSR-synthesized CeO_x-Pd/C catalysts (Figure S4, Supporting Information), which are comparable to other Pd-CeO_2 catalysts synthesized using different methods in the literature (2–5 nm).[34,36] The uniform distribution of CeO_x on Pd was also observed for 0.38 CeO_x-Pd/C by STEM/EDS maps and it is in line with a lower Pd(0)/Pd(IV) ratio obtained from XPS (Figure 2e–h).

The STEM/EDS maps (Figure 2e–h), high-angle annular dark-field (HAADF)-STEM image (**Figure 3**a) and ultra-high-resolution electron energy loss spectroscopy (EELS) maps (Figure 3b–e) of 0.38 CeO_x-Pd/C catalysts show that CeO_x is in intimate contact with Pd. The intensity ratio of I_{M5}/I_{M4} bands of CeO_x suggests that most CeO_x is in the form of CeO_2 (Figure 3f). However, the presence of Ce^{3+} cannot be ruled out, specially near the surface of the particles.[49] From the single nanoparticle EELS map of 0.38 CeO_x-Pd/C, it is seen that CeO_x

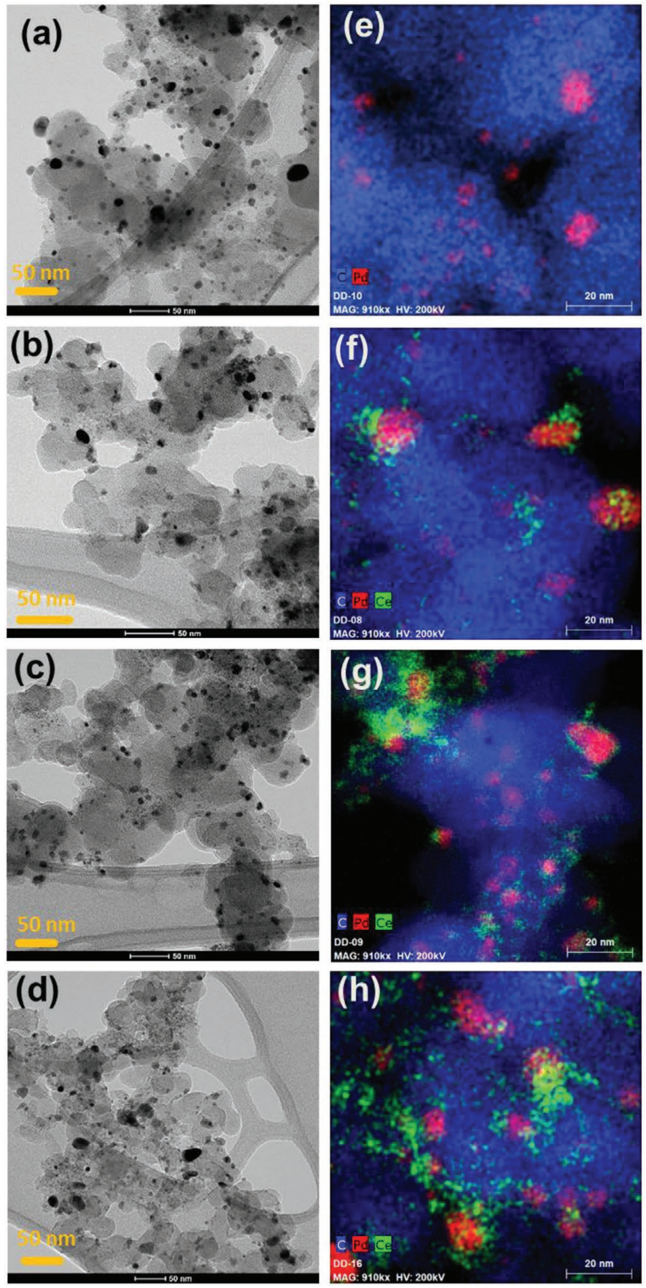

Figure 2. HRTEM images of a) Pd/C, b) 0.24 CeO_x-Pd/C, c) 0.38 CeO_x-Pd/C, d) 0.59 CeO_x-Pd/C, and the e–h) corresponding overlay STEM/EDS maps. The scale bar in the HRTEM images (a–d) is 50 and 20 nm in (e–h).

is forming a shell around the Pd core. The interfacial contact area seems to be much higher than other previously reported Pd-CeO_2 catalysts synthesized by other methods,[34–36] suggesting that the CSR method resulted in a higher selective deposition of CeO_x on Pd. The interface between Pd and CeO_x is further evidenced by high-resolution HAADF-STEM images shown in **Figure 4**. It is worthwhile mentioning that analyzing the particle size distribution of CeO_x is challenging because it does not form well-defined nanoparticles, and its contrast is similar to that of Pd, as can be seen in the HAADF-STEM micrographs (Figure 4) and the EELS color mapping (Figure 3).

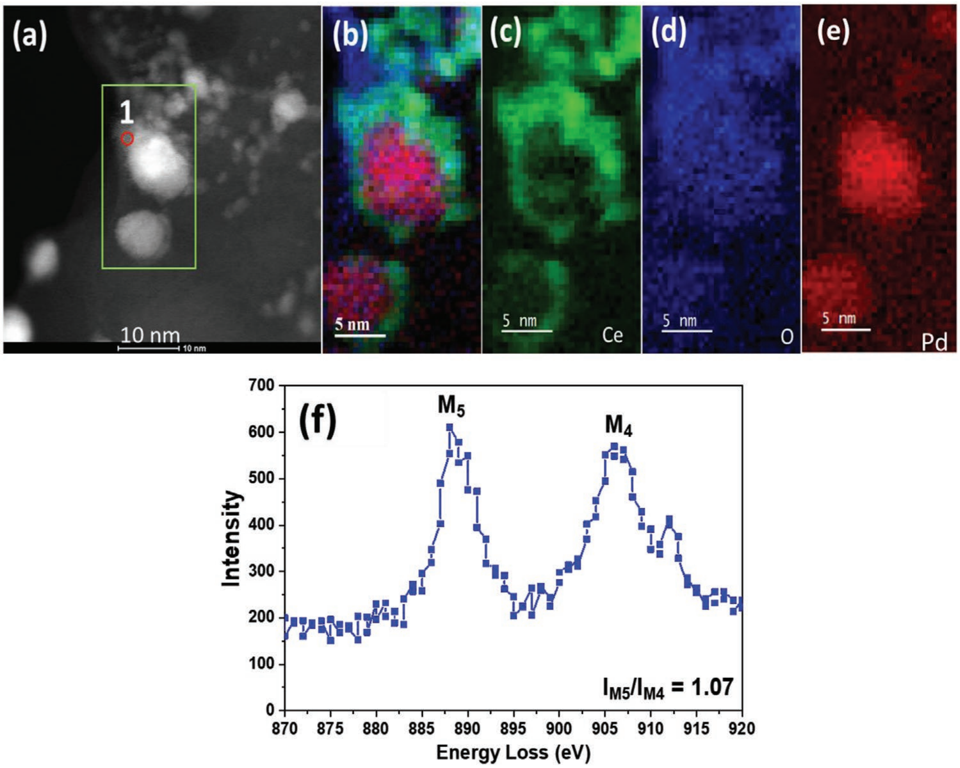

Figure 3. a) High-resolution HAADF-STEM image and the b–e) corresponding EELS mapping of 0.38 CeO_x-Pd/C. The overlay map (b) and green, blue, and red colors in maps (c–e) correspond to Ce, O, and Pd, respectively. f) EELS spectra of CeO_x recorded at point 1 shown in (a).

Moreover, we were able to calculate the interplanar spacing from the CeO_2 reflections as shown in Figure 4. The additional (110) reflection is observed for the 0.38 CeO_x-Pd/C catalysts (Figure 4b). The different lattice spacing of Pd and CeO_2 phases of the n CeO_x-Pd/C catalysts (Tables S2, S3, and S4, Supporting Information), together with the HRTEM images and corresponding diffraction patterns shown in Figures S5, S6, and S7 in the Supporting Information, allowed us to further investigate the interface.

In an attempt to quantify this interface, the intimate interfacial contact area between Pd and CeO_x was calculated using ten different STEM maps for each sample. The CeO_x-Pd contact area of the different synthesized catalyst was segmented and calculated using Image J software. Detailed calculations and representative STEM maps are included in the Supporting Information (see Tables S5, S6, S7 and Figures S8, S9, S10 in the Supporting Information). The calculated interfacial contact areas between Pd and CeO_x

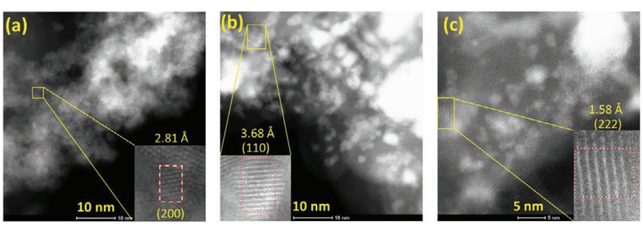

Figure 4. HAADF-STEM images of a) 0.24 CeO_x/Pd/C, b) 0.38 CeO_x/Pd/C, and c) 0.59 CeO_x/Pd/C. Inset show interplanar spacing from reflections (200), (110), and (222) corresponding to CeO_2.

of 184.8, 259.7, and 250.3 nm^2 were obtained for 0.24 CeO_x-Pd/C, 0.38 CeO_x-Pd/C, and 0.59 CeO_x-Pd/C, respectively; which represents an average percentage interfacial contact area of 17.8%, 20.8%, and 18.9%, respectively. The interfacial contact area increases with the addition of CeO_x, reaching a maximum at 0.38 CeO_x-Pd/C, and decreases upon further addition of CeO_x. This is consistent with the formation of larger islands upon the addition of CeO_x, as shown before, observed for 0.59 CeO_x-Pd/C. This can be explained by the complete coverage of the Pd surface and the increased deposition of CeO_x onto the support. As previously stated, in order to achieve the best catalytic performance, it is believed that a high interfacial contact between Pd and CeO_x is required, as it enhances the OH^- spillover from CeO_x to Pd. This is further confirmed by electrochemical measurements as shown below.

The electrochemical behavior of CeO_x-Pd/C catalysts in 0.1 M KOH electrolyte is shown in **Figure 5**. As can be seen in Figure 5a, the CVs of the synthesized catalysts exhibited typical features of Pd, with a well-defined hydrogen adsorption/desorption region within 0.05–0.45 V,[34–36] oxide formation at potentials above 0.80 V,[34] and oxide reduction region within 0.60–0.70 V.[34,38,39] The H-desorption (H_{des}) peak in the potential window of 0.05–0.45 V gradually increases up to Ce/Pd bulk atomic ratio of 0.38 and decreases after that. Interestingly, the H_{des} peak at 0.33 V in the case of Pd/C is less pronounced in comparison to that in CeO_x-Pd/C catalysts. In addition, there is a border H_{des} peak observed at >0.60 V with Pd/C (see Figure S11a in the Supporting Information). The sharp H_{des} peak of 0.38 CeO_x-Pd/C starts at slightly lower potential (0.32 V) in comparison to Pd/C (0.33 V). This sharp H_{des} peak

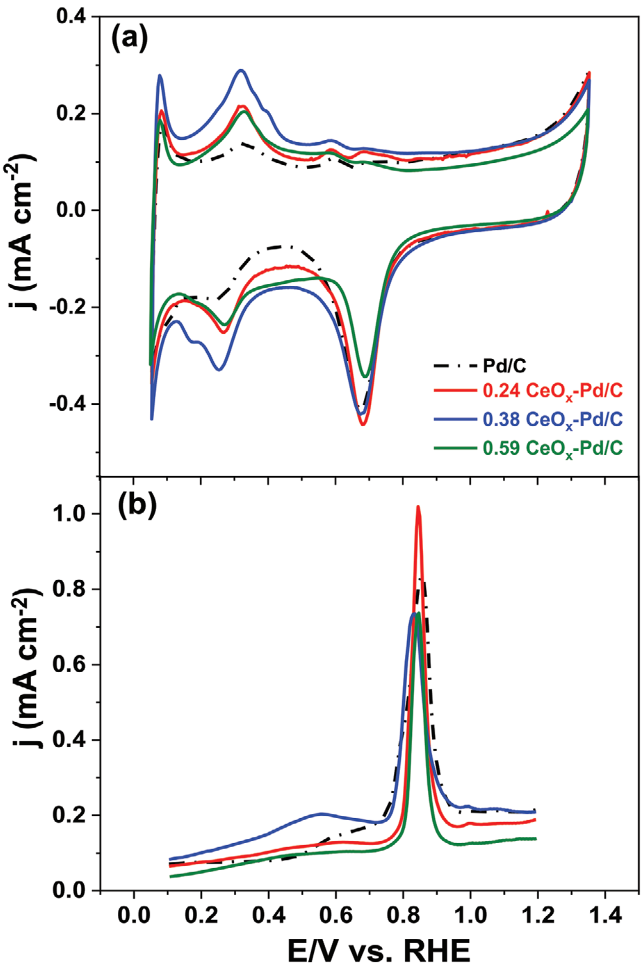

Figure 5. Overlaid cyclic voltammograms of the CSR-synthesized CeO_x-Pd/C catalysts (and Pd/C as the reference) at the sweep rate of 20 mV s^{-1} in a) argon-saturated 0.1 м KOH and b) the corresponding CO stripping voltammograms at a scan rate of 20 mV s^{-1} in 0.1 м KOH electrolyte.

with CeO_x-Pd/C catalysts is believed to be the weaker Pd-H interaction of CeO_x-Pd catalysts compared to Pd/C, which is consistent with the decrease in the HBE recently calculated by DFT by Bellini et al.[37] The well-defined oxide formation and reduction features were not observed in some of the previously reported Pd/C-CeO_x catalysts,[35–37] which might be due to the high CeO_x content (above 50 at%). It is important to mention that all the CeO_x-Pd/C catalysts are stable during cycling (see Figure S11 in the Supporting Information).

Table 4. CO stripping peak potentials and electrochemical surface area of Pd/C and CSR-synthesized CeO_x-Pd/C catalysts estimated from both CO stripping and PdO reduction charge.

Catalyst	E_{peakCO} [V]	$ECSA_{CO}$ [m^2 g^{-1}_{Pd}]	$ECSA_{PdO}$ [m^2 g^{-1}_{Pd}]
Pd/C	0.857	54.8	46.9
0.24 CeO_x-Pd/C	0.846	55.5	49.7
0.38 CeO_x-Pd/C	0.832	52.4	46.3
0.59 CeO_x-Pd/C	0.841	36.5	26.2

The overlaid CO-stripping voltammograms of CSR-synthesized CeO_x-Pd/C catalysts are shown in Figure 5b. A sharp CO stripping peak is observed for all the catalysts at ≈0.83–0.85 V, which is characteristic of precious metals.[20,23] The highest CO-stripping peak potential of 0.857 V is observed for Pd/C and gradually decreases with an increase in the Ce/Pd ratio in the catalyst. The maximum shift of 0.025 V to lower potentials is calculated with the 0.38 CeO_x-Pd/C, in line with the highest interfacial area calculated between CeO_x and Pd. Besides, we see the broad CO-stripping peak at the lower potential of ≈0.3–0.7 V on CSR-derived catalysts which suggest the presence of OH_{ad} at lower potential.[20] This broad peak is more pronounced with 0.38 CeO_x-Pd/C, which is in line with the highest calculated interfacial contact area and thus the efficient OH^- spillover from CeO_x to Pd. The shift in the CO stripping peak potential to a lower value is attributed to the presence of OH_{ad} at lower potentials, which promotes the Volmer step and thus facilitates the HOR, in line with OH^- transfer from CeO_x to Pd.[20] In order to compare the surface HOR activity, accurate electrochemically active surface area (ECSA) determination of these CSR-synthesized catalysts is necessary. Due to the difficulty in separating the hydrogen adsorption and absorption phenomena with Pd,[66,67] the ECSA estimated from the H_{upd} charge may not lead to reliable results. Therefore, the ECSA was determined from both PdO reduction and CO stripping charges. ECSA values estimated from both methods are comparable and follow a similar trend (**Table 4**). ECSA decreases with an increase in the Ce/Pd ratio of the CeO_x-Pd/C catalysts. This decrease is attributed to the surface Pd coverage by CeO_x.

The HOR LSVs of the CeO_x-Pd/C catalysts are shown in **Figure 6**. The HOR current starts at 0.0 V and reached to limiting current value of ≈2.75 mA cm^{-2}. The HOR limiting current observed at 0.2 V with both 0.24 CeO_x-Pd/C and 0.38 CeO_x-Pd/C catalysts reflects the influence of the mass-transport limitation. Importantly, the HOR current onset potential starts at

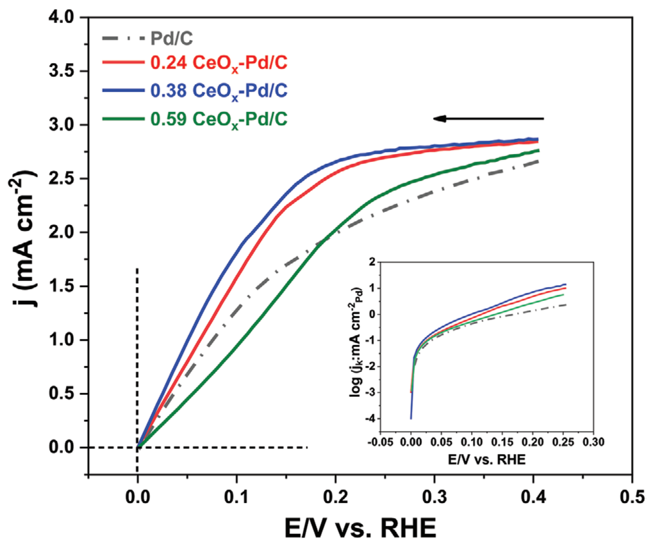

Figure 6. HOR polarization curves of Pd/C and CSR-synthesized CeO_x-Pd/C in H_2-saturated 0.1 м KOH at the sweep rate of 2 mV s^{-1} with a rotation rate of 1600 rpm. Inset shows electrochemical surface area normalized HOR polarization Tafel plots in the kinetic potential range. The solid arrow line shows the direction of the LSV scan.

Table 5. Kinetic HOR parameters of the Pd/C and CSR-synthesized CeO_x-Pd/C catalysts in 0.1 M KOH solution.

Catalyst	$i_{o,m}$ [mA mg^{-1}_{Pd}]	$j_{o,s}$ [mA cm^{-2}_{Pd}]	Tafel slope [mV $decade^{-1}$][a)]
Pd/C	20.84	0.045	218.0
0.24 CeO_x-Pd/C	45.08	0.092	131.5
0.38 CeO_x-Pd/C	51.54	0.118	129.3
0.59 CeO_x-Pd/C	20.11	0.077	144.1

[a)]The Tafel slopes were calculated in the overpotential range of 100–250 mV.

0.0 V with all the catalysts. From the LSVs, it can be concluded that the HOR current increases sharply with the rise in the Ce/Pd bulk ratio to 0.38, and after that, a decrease in the HOR current is noticed. The LSV half-wave potential of 0.38 CeO_x-Pd/C catalyst is 75 mV, which is 20 mV lower than Pd/C (95 mV) and the lowest among the reported Pd-CeO_2 catalysts.[35,40] In order to truly compare the performance of these catalysts, the exchange current ($j_{o,s}$ and $i_{o,m}$) and Tafel slopes are calculated and given in **Table 5**. The HOR specific exchange current ($i_{o,m}$) increases with an increase in Ce/Pd bulk atomic ratio from 0 up to 0.38 and then decreases with the further addition of CeO_x (Table 5). The corresponding kinetic current density (j_k) and Tafel plots of the CSR-synthesized CeO_x-Pd/C catalysts are shown in Figure S12 in the Supporting Information and inset to Figure 6, respectively. A volcano-like relationship is observed with HOR kinetic current at 100 mV (see Figure S12 in the Supporting Information) and a similar trend is also noticed with both $i_{o,m}$ and $j_{o,s}$. The maximum $j_{k,s}$ and $i_{k,m}$ is observed with 0.38 CeO_x-Pd/C in line with results from $j_{o,s}$ and $i_{o,m}$. The lowest Tafel slopes of 129.3 mV $decade^{-1}$ is observed for the 0.38 CeO_x-Pd/C catalyst which is 1.7 times lower than Pd/C (218 mV $decade^{-1}$) with the highest HOR specific exchange current, which suggests that the improved intrinsic kinetics of HOR and Volmer step is the rate-determining step on this class of catalysts.[18]

The HOR specific exchange current ($i_{o,m}$) of the catalysts reported here are compared to previously reported Pd/C-CeO_2 catalysts in **Figure 7**. The catalyst with optimum Ce/Pd bulk atomic ratio of 0.38 exhibited an $i_{o,m}$ of 51.5 mA mg^{-1}_{Pd}. This 0.38 CeO_x-Pd/C catalyst exhibit the highest $i_{o,m}$ from all previously reported Pd-CeO_2 catalysts (see the summary of all values in Table S8 in the Supporting Information), showing that CSR is a promising method to achieve high contact between CeO_x and Pd, and in turn, a high electrochemical activity towards HOR. It is worth noting that the CeO_x loading in 0.38 CeO_x-Pd/C is only 4 wt% (27.8 wt% considering only CeO_x-Pd), which further demonstrates that the CSR method results in highly active catalysts with a minimum amount of CeO_x added. The interfacial contact area as a function of the Ce/Pd bulk atomic ratio is shown in **Figure 8**. The calculated $i_{o,m}$ is correlated with the highest interfacial area and Ce/Pd ratio as shown in the high-resolution STEM micrographs. As the coverage of CeO_x increases, the interfacial area increases and thus, the HOR activity up to Ce/Pd of 0.38, followed by an activity decrease with a further rise in Ce/Pd ratio to 0.59. The decrease in activity is mainly attributed to the deposition of CeO_x onto carbon rather than Pd and the formation of large CeO_x nanoislands, as confirmed by XPS and STEM analyses.

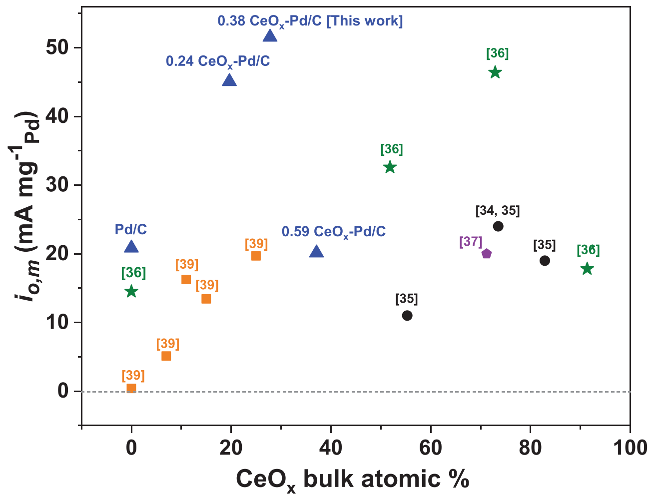

Figure 7. The effect of CeO_x bulk content (at% of CeO_x into the CeO_x-Pd catalyst) on the specific exchange current values for the Pd/C and CSR-synthesized CeO_x-Pd/C catalysts (blue triangular), compared to the previously published data ([34–37,39]). The bulk at% of CeO_x is calculated with respect to the sum of Pd and CeO_x.

Due to its high specific exchange current, the 0.38 Pd-CeO_x/C catalyst was selected to be tested in a fuel cell. The H_2–O_2 AEMFC performance of the 0.38 Pd-CeO_x/Ccatalyst (and its comparison with Pd/C catalyst) is shown in **Figure 9**a,b. The

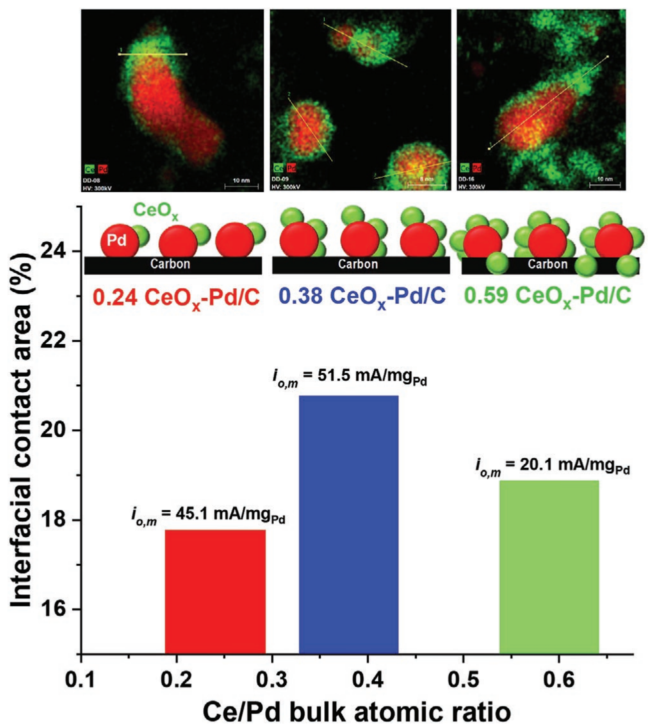

Figure 8. Interfacial contact area as a function of the Ce/Pd bulk atomic ratio. The scales in the high-resolution STEM maps of Pd and Ce are 10, 8, and 10 nm. The scheme shows the selective deposition of CeO_x nanoislands onto carbon-supported Pd nanoparticles by CSR: 0.24 CeO_x-Pd/C, 0.38 CeO_x-Pd/C, and 0.59 CeO_x-Pd/C. The black rectangle represents the carbon support, and Pd nanoparticles and CeO_x nanoislands are represented in red and green, respectively.

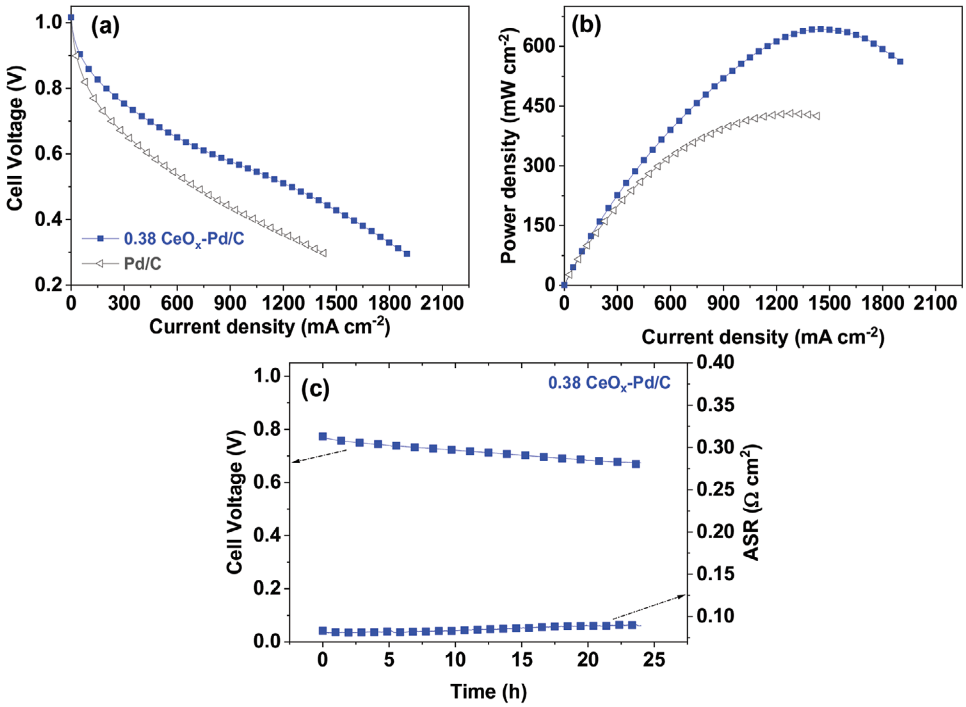

Figure 9. H_2–O_2 AEMFC performance of CSR-synthesized 0.38 CeO_x-Pd/C as compared to Pd/C: a) polarization curve, b) power density curve as a function of current density, and c) AEMFC stability test at constant 200 mA cm^{-2} load. Anode catalyst loading of 0.55 mg_{Pd} cm^{-2} (0.38 CeO_x-Pd/C) and 0.65 mg_{Pd} cm^{-2} (Pd/C), Pt/C cathode catalyst (0.7 mg_{Pt} cm^{-2}). Cell temperature 333 K, H_2 and O_2 flow rates of 1000 mL min^{-1}, no backpressure.

AEMFC experiments were repeated twice to ensure reproducibility. A peak power density of 1169 mW cm^{-2} mg_{Pd}^{-1} is achieved with the 0.38 CeO_x-Pd/C catalyst, 1.8 times higher than that achieved with the Pd/C (663 mW cm^{-2} mg_{Pd}^{-1}). This is consistent with the higher $i_{o,m}$ of 0.38 CeO_x-Pd/C as compared to Pd/C (Table 4). This performance is also higher as compared to other similar catalysts, as shown in a comparison of the AEMFC performance of previously reported Pd-based catalysts (see Table S9 in the Supporting Information).[32,34,35,68,69] Moreover, the IR-corrected single-cell AEMFC peak power density increased significantly, reaching to record high 1565 mW cm^{-2} mg_{Pd}^{-1} at 333 K, which shows a promising impact in the future research and potential practical applications (Figure S13, Supporting Information). The stability test of the cell based on 0.38 CeO_x-Pd/C catalyst is shown in Figure 9c. The AEMFC was tested at 200 mA cm^{-2} constant current density load for 24 h, showing a stable voltage output, suggesting that the 0.38 CeO_x-Pd/C catalyst has good stability under the harsh AEMFC environment.

3. Conclusion

CeO_x-Pd/C catalysts with various Ce/Pd ratios were synthesized by selective deposition of CeO_x onto carbon-supported Pd/C nanoparticles by controlled surface reactions (CSR). The higher surface Ce/Pd atomic ratio when compared to the bulk Ce/Pd, demonstrated the surface affinity of the CSR method. EELS and high-resolution STEM images revealed the core-shell structure of the CeO_x-Pd nanoparticles and Ce^{4+} mainly present in CeO_x, respectively. We have clearly shown that CeO_x nanoparticles are in intimate contact with Pd, as seen from the high-resolution STEM images recorded on single particles. A very high interfacial contact area between CeO_x and Pd nanoparticles was achieved, and for the first time, it was also calculated. Most interestingly, this interfacial contact area was found to be directly correlated to the HOR activity of the CeO_x-Pd/C catalysts. The CSR method used in this work yielded the catalyst with the highest HOR specific activity ever measured for Pd-CeO_x catalysts—high value of 51.5 mA mg^{-1}_{Pd} was measured for the 0.38 CeO_x-Pd/C. This was explained by the improved distribution of CeO_x onto Pd, the higher concentration of Pd(IV) sites, as well as the higher interfacial contact area between CeO_x and Pd nanoparticles. Moreover, the 0.38 CeO_x-Pd/C catalyst showed a very high performance while tested in a fuel cell. The H_2–O_2 AEMFC made with this catalyst exhibited a peak power density of 1169 mW cm^{-2} mg_{Pd}^{-1} at 333 K, significantly higher than other cells with similar HOR catalysts.

4. Experimental Section

Materials: For the catalyst synthesis, palladium (II) acetate (Acros Organics, 99.9%), dichloromethane (Acros Organics, 99.6%, ACS reagent, stabilized with amylene), tris(cyclopentadienyl)cerium(III) (STREM Chemicals, Inc. 99.9%), anhydrous tetrahydrofuran (Sigma-Aldrich, ≥99.9%, inhibitor-free), and Vulcan XC-72 carbon (Cabot) were used. For the electrolyte and catalysts ink preparation, potassium hydroxide flakes (85.0–100.5% w/w AR grade, Bio-Lab, Israel), isopropyl alcohol (99.8 assay from the Gadot group, Israel), and Nafion ionomer perfluorinated resin (10 wt% in water from Sigma-Aldrich) were used. For the fuel cell electrode fabrication and testing, Toray Paper (060 – TGP-H-060 with 5 wt% PTFE wetproofing from Fuel Cell Store), Vulcan XC-72 carbon (Cabot), and 40% platinum on carbon black (HiSPEC 4000 from Alfa Aesar) were used. Argon, oxygen, nitrogen and hydrogen gases of purity 99.999% were purchased from Maxima, Israel. Carbon monoxide gas of purity 99.99% (Gas Technologies, Israel) was used for the CO stripping experiments. High purity (18.2 Ω) double-distilled water was used. All the chemicals were used without any further purification.

Catalyst Synthesis: A series of CeO_x-Pd/C catalysts were synthesized by selective deposition of CeO_x onto carbon-supported Pd nanoparticles by controlled surface reactions (CSR).[57–61,70–77] First, a 10 wt% Pd/C catalyst was prepared by wet impregnation by adding a solution of 0.84 g of palladium (II) acetate in 100 mL of dichloromethane to 3.6 g of Vulcan XC-72 carbon. The mixture was stirred in an open vessel at 323 K to evaporate the solvent. Once dry, the catalyst was reduced in a Schlenk tube at 343 K (heating ramp of 0.8 K min^{-1}) for 2 h under H_2 flow. After the reduction, the Schlenk tube was sealed and transferred to a glove box under an ultrapure argon atmosphere to prevent oxidation. Then, tris(cyclopentadienyl)cerium(III) was used as a precursor for the addition of CeO_x using sequential CSR cycles. For each CSR cycle, 0.2 g of tris(cyclopentadienyl)cerium (III) was dissolved into 90 mL of anhydrous tetrahydrofuran under argon atmosphere in the glove box, then 15 mL of the CeO_x precursor solution was added to 1 g of the reduced Pd/C catalyst. The Schlenk tube was then sealed and stirred for 3 h, after which the solution becomes clear, indicating the total uptake of the precursor. Then, the solvent was evaporated using Schlenk techniques[57] and the tube was filled with argon and sealed to carry out a second thermal treatment. The catalyst was then heated at 573 K (heating ramp of 1.6 K min^{-1}) for 2 h under H_2 flow. This second thermal treatment removes the ligands of the CeO_x precursor in order to obtain an effective interaction between Pd and CeO_x, while maintaining Pd reduced for subsequent deposition cycles. After the last cycle was applied, the catalysts were reduced in H_2 flow at 573 K (heating ramp of 1.6 K min^{-1}) for 2 h and used without prior passivation. Every CSR cycle provides a theoretical atomic ratio of Ce/Pd of 0.13 (see Supporting Information for calculation details). A series of CeO_x-Pd/C catalysts with different number of CSR cycles were prepared aiming to obtain different (theoretical) Ce/Pd atomic ratios: 0.26, 0.39, and 0.65. For the electrochemical measurements, the catalysts were grounded with a mortar and pestle to obtain uniform powders.

Catalysts Characterization: The composition of the synthesized catalysts was determined via Inductively Coupled Plasma–Atomic Emission Spectrometry (ICP-AES). Samples (≈30 mg) were fused with sodium peroxide over a Bunsen burner, then dissolved in water. The resultant solutions were then acidified and analyzed using an ICP-OES Optima 5300 V spectrometer.[78,79] X-ray diffraction (XRD) data were collected using a Rigaku Smartlab diffractometer with $CuK_{\alpha 1}$ X-ray source ($\lambda = 0.15406$ nm). The X-ray diffractograms were recorded at medium resolution parallel beam geometry at a tube current of 150 mA and a tube voltage of 45 kV, in $\theta/2\theta$ scan mode with a scan rate of 2° min^{-1} in 0.01° steps, in a range of diffraction angles from 20° to 90°. Phases were identified via matching results with the International Centre for Diffraction Data (ICDD) PDF4+ (2018) database. Electron microscopy images and analyses were conducted in a Thermo Scientific™ TalosF200 × 200 kV D6329 XTwin Transmission Electron Microscope (TEM), using both Bright Field and High Angle Annular Dark Field (HAADF) Scanning Transmission Electron Microscopy (STEM) modes. The samples were first dispersed in 50 v/v % of isopropyl alcohol and distilled water, then ultrasonicated using a 2510R-DTH Bransonic^R Ultrasonic Cleaner for 15–30 min (130 W, 40 kHz) and deposited on a holey carbon-coated Cu grid for TEM characterization, followed by drying for 30 min under an ultraviolet lamp. Energy Dispersive Spectroscopy (EDS) with a ChemiSTEM™ technology system contained within the TEM was used for elemental analysis of the catalyst samples, using hyper-mapping collected by an ESPRIT Microanalysis Software. The mapping was performed using a screen current of 2.5 nA, beam dwells time of 1000 µs per pixel for one mapping cycle. For high-resolution STEM imaging, the samples were studied by TEM with Titan Themis 60-300. The TEM images were performed at 300 keV and with its DCorr+ probe corrector that corrects condenser spherical aberration higher than 25 mrad, enabling a spatial resolution down to 0.08 nm with 25 mrad convergence angle for its atomic resolved HAADF-STEM imaging. For high-resolution Electron Energy-loss Spectroscopy (EELS) measurements, the data were collected through Gatan GIF Quantum 963 spectrometer system attached to Themis operating at 300 kV in STEM mode with EELS collection angle of 50 mrad. A 0.5 eV per channel dispersion was used to map elemental distribution in a wide energy range and 0.05 eV per channel dispersion was selected for the highest energy resolution (1.1 eV). An X-ray photoelectron spectroscopy (XPS) equipment with a monochromated Al source (1486.6 eV, Kratos Axis) was used to record the XPS spectra. The XPS resolution was about 0.6 eV when the pass energy of 20 eV was used. The energy scale was calibrated with Ag $3d_{5/2}$ that was assigned at 368.21 eV. No charge neutralizer was used as all the samples were conductive.

Electrochemical Characterization: Electrochemical measurements of the synthesized catalysts were performed in a conventional three-electrode rotating disc electrode (RDE) set-up using a WaveDriver potentiostat in an electrochemical cell from Pine Instruments (water-jacketed, five compartment glass cell). All the RDE measurements were performed at 298 ± 0.2 K. The catalyst-coated glassy carbon disc was used as a working electrode, a standard Pt counter electrode was immersed inside a fritted glass tube to avoid any Pt dissolution, and Hg/HgO (4.24 м KOH) was used as a reference electrode (both from Pine Instruments). The potential of the reference electrode was calibrated against the reversible hydrogen electrode (RHE) (880 mV).

The catalyst ink was prepared by mixing 10 mg of catalyst, 2.5 mL of de-ionized water, 5.5 mL of isopropyl alcohol, and 9.52 µL of Nafion ionomer (10 wt% solution in water). The mixture was sonicated at 100% intensity (580 W) in a Grant XUBA3 ultrasonic bath filled with water and ice to keep the temperature below 278 K for 30 min to form a uniform catalyst ink. The homogenous ink was drop-coated on a glassy carbon disc working electrode to obtain a nominal loading of 13 μg_{Pd} cm^{-2}, and dried in an ambient atmosphere for 1 h. Prior to hydrogen oxidation measurements, the electrode was cycled in 0.1 м KOH solution at the sweep rate of 100 mV s^{-1} from 0.0 to 1.2 V versus RHE for 50 cycles, to get a reproducible voltammogram. Then a cyclic voltammogram (CV) was recorded from 0.05 to 1.35 V at the sweep rate of 20 mV s^{-1} for the estimation of electrochemical surface area (ECSA) from PdO reduction using Equation (1).[80,81] The upper potential of CV was selected in such a way that the surface area estimation corresponds to the monolayer oxide coverage on the Pd surface.[34] For the ECSA estimation using CO-stripping voltammograms, the electrolyte solution was saturated with CO for 10 min, followed by CO adsorption at 0.025 V for 10 min. Then the solution was saturated with argon at 0.025 V for 30 min to remove the CO from the electrolyte while maintaining the same potential load. The CO stripping voltammograms were then recorded from 0.0 to 1.2 V at the sweep rate of 20 mV s^{-1}. The ECSA from the CO stripping charge was then estimated using Equation (2)

$$ECSA_{PdO} = \frac{\text{PdO reduction charge}}{\text{scan rate} \times \text{specific charge} \times \text{catalyst loading}} \tag{1}$$

$$ECSA_{CO} = \frac{\text{CO stripping charge}}{\text{scan rate} \times \text{specific charge} \times \text{catalyst loading}} \tag{2}$$

where, ECSA is in $cm^2\ g^{-1}_{Pd}$, PdO reduction charge in C cm^{-2}_{geom}, scan rate in V s^{-1}, catalyst loading is in $g_{Pd}\ cm^{-2}_{geom}$ (the measured Pd content from ICP-AES is used), and CO stripping charge in C cm^{-2}_{geom}. A specific charge of 420×10^{-6} C cm^{-2} was used for ECSA determination using PdO reduction[80,81] and CO stripping charges.[82]

HOR linear sweep voltammograms (LSVs) were recorded with rotation rates from 2000 to 900 rpm in H_2-saturated 0.1 м KOH solution at a scan rate of 2 mV s^{-1}. The kinetic current density is usually estimated from the Koutecky-Levich equation as follows[83,84]

$$\frac{1}{i} = \frac{1}{i_k} + \frac{1}{i_d} \quad (3)$$

where i is the measured current, i_k is the kinetic current, and i_d is the diffusion limiting current.

i_k was derived from measured diffusion limiting current at single rotation speed (typically 1600 rpm) using Equation (3) when the loading of catalyst was less than 15 µg cm^{-2}.[83] Both the mass ($i_{o,m}$) and surface ($j_{o,s}$) exchange current densities were calculated from the micro-polarization method where the Butler-Volmer equation approaches linear behavior[19,36] (Equation (4)) within a very small overpotential range (<15 mV), by dividing the exchange current (i_0) to ECSA estimated from PdO reduction charge and mass of Pd obtained from ICP-AES, respectively

$$i_k = i_o \times \frac{F\eta}{RT} \quad (4)$$

where F is the Faraday constant (96485 C mol^{-1}), η is the overpotential (V), T is the temperature (298 K), and R is the universal gas constant (8.314 J mol^{-1} K^{-1}). All the electrochemical measurements were repeated twice to ensure reproducibility.

Anion Exchange Membrane Fuel Cells: Gas diffusion electrodes (GDEs) were prepared for both anode and cathode for the fabrication of anion exchange membrane fuel cells. Both the anode and cathode electrodes consisted of three layers: a gas diffusion layer (GDL) (Toray Paper), a microporous layer (MPL) of carbon black (Vulcan XC-72), and a catalyst layer. The details of the anode and cathode ink preparations were given in the Supporting Information. Each electrode was prepared by spray coating the MPLs directly onto the GDLs, then adding the respective cathode and anode catalyst inks on top of the MPLs. Two 5 cm^2 active area fuel electrodes cells were made using 40 wt% Pt/C as the cathode catalyst (0.7 mg$_{Pt}$ cm^{-2}) and either CSR-synthesized CeO_x-Pd/C (0.55 mg$_{Pd}$ cm^{-2}) or Pd/C (0.64 mg$_{Pd}$ cm^{-2}) catalysts as anodes. A 16 cm^2 piece of poly(ethylene-*co*-tetrafluoroethylene)-benzyltrimethylammonium chloride (ETFE-BTMA) radiation grafted anion exchange membrane[85–88] was sandwiched between the anode and cathode electrodes to make two membrane electrode assemblies (see the Supporting Information for more details). The AEMFCs were tested at the same conditions in an 850E Scribner Associates fuel cell test station. Polarization curves were recorded at 333 K under O_2 flow at the cathode (1000 mL min^{-1}, dew point 328 K) and H_2 flow at the anode (1000 mL min^{-1}, dew point 325 K).

Supporting Information

Supporting Information is available from the Wiley Online Library or from the author.

Acknowledgements

This work was partially funded by the Nancy & Stephen Grand Technion Energy Program (GTEP); by the European Union's Horizon 2020 research and innovation program [Grant No. 721065]; by the Ministry of Science, Technology & Space of Israel through Grant No. 3-12948; by the Israel Science Foundation (ISF) [Grant No. 1481/17]; by the Ministry of National Infrastructure, Energy and Water Resources of Israel [Grant No. 3-13671], and by the UConn-Technion Energy Collaboration initiative, supported by the Satell Family Foundation, the Maurice G. Gamze Endowed Fund (at the American Technion Society), Larry Pitt and Phillis Meloff, The Eileen and Jerry Lieberman UConn/Israel Global Partnership Fund and the Grand Technion Energy Program (GTEP). The UConn-ThermoFisher Scientific Center for advanced microscopy and materials analysis (CAMMA) is acknowledged for the EELS and high-resolution STEM analysis. The authors would also like to acknowledge the financial support of Melvyn & Carolyn Miller Fund for Innovation, as well as the support of Planning & Budgeting Committee/ISRAEL Council for Higher Education (CHE) and Fuel Choice Initiative (Prime Minister Office of ISRAEL), within the framework of "Israel National Research Center for Electrochemical Propulsion (INREP)." B.J.A. and A.C.A.-R. would like to acknowledge the University of Toledo for the financial support through the faculty start-up fund. Finally, the authors would like to thank Prof. John Varcoe (Surrey University, UK) for the generous supply of his membrane materials used in this study. The authors also acknowledge funding of a PRIN 2017 Project funded by the Italian Ministry MUIR (Grant No. 2017YH9MRK).

Conflict of Interest

The authors declare no conflict of interest.

Keywords

anion exchange membrane fuel cells, controlled surface reactions, electrocatalysts, hydrogen oxidation reaction, palladium-ceria

Received: March 5, 2020
Revised: May 21, 2020
Published online: July 23, 2020

[1] J. R. Varcoe, P. Atanassov, D. R. Dekel, A. M. Herring, M. A. Hickner, P. A. Kohl, A. R. Kucernak, W. E. Mustain, K. Nijmeijer, K. Scott, T. Xu, L. Zhuang, *Energy Environ. Sci.* **2014**, *7*, 3135.
[2] D. R. Dekel, *J. Power Sources* **2018**, *375*, 158.
[3] S. Gottesfeld, D. R. Dekel, M. Page, C. Bae, Y. Yan, P. Zelenay, Y. S. Kim, *J. Power Sources* **2018**, *375*, 170.
[4] S. Willdorf-Cohen, A. N. Mondal, D. R. Dekel, C. E. Diesendruck, *J. Mater. Chem. A* **2018**, *6*, 22234.
[5] D. R. Dekel, M. Amar, S. Willdorf, M. Kosa, S. Dhara, C. E. Diesendruck, *Chem. Mater.* **2017**, *29*, 4425.
[6] C. E. Diesendruck, D. R. Dekel, *Curr. Opin. Electrochem.* **2018**, *9*, 173.
[7] S. Pusara, S. Srebnik, D. R. Dekel, *J. Phys. Chem. C* **2018**, *122*, 11204.
[8] D. R. Dekel, I. G. Rasin, S. Brandon, *J. Power Sources* **2019**, *420*, 118.
[9] A. Zhegur, N. Gjineci, S. Willdorf-Cohen, A. N. Mondal, C. E. Diesendruck, N. Gavish, D. R. Dekel, *ACS Appl. Polym. Mater.* **2020**, *2*, 360.
[10] I. Zadok, D. R. Dekel, S. Srebnik, *J. Phys. Chem. C* **2019**, *123*, 27355.
[11] J. Fan, S. Willdorf-Cohen, E. M. Schibli, Z. Paula, W. Li, T. J. G. Skalski, A. T. Sergeenko, A. Hohenadel, B. J. Frisken, E. Magliocca, W. E. Mustain, C. E. Diesendruck, D. R. Dekel, S. Holdcroft, *Nat. Commun.* **2019**, *10*, 2306.
[12] Y. Zheng, T. J. Omasta, X. Peng, L. Wang, J. R. Varcoe, B. S. Pivovar, W. E. Mustain, *Energy Environ. Sci.* **2019**, *12*, 2806.
[13] S. Srebnik, S. Pusara, D. R. Dekel, *J. Phys. Chem. C* **2019**, *123*, 15956.
[14] N. Ziv, A. N. Mondal, T. Weissbach, S. Holdcroft, D. R. Dekel, *J. Membr. Sci.* **2019**, *586*, 140.
[15] N. Ziv, W. E. Mustain, D. R. Dekel, *ChemSusChem* **2018**, *11*, 1136.
[16] D. R. Dekel, *Curr. Opin. Electrochem.* **2018**, *12*, 182.
[17] E. S. Davydova, S. Mukerjee, F. Jaouen, D. R. Dekel, *ACS Catal.* **2018**, *8*, 6665.
[18] C. A. Campos-Roldán, N. Alonso-Vante, *Electrochem. Energy Rev.* **2019**, *2*, 312.
[19] J. Durst, A. Siebel, C. Simon, F. Hasché, J. Herranz, H. A. Gasteiger, *Energy Environ. Sci.* **2014**, *7*, 2255.
[20] J. Li, S. Ghoshal, M. K. Bates, T. E. Miller, V. Davies, E. Stavitski, K. Attenkofer, S. Mukerjee, Z. F. Ma, Q. Jia, *Angew. Chem., Int. Ed.* **2017**, *56*, 15594.
[21] W. Sheng, M. Myint, J. G. Chen, Y. Yan, *Energy Environ. Sci.* **2013**, *6*, 1509.

[22] D. Strmcnik, M. Uchimura, C. Wang, R. Subbaraman, N. Danilovic, D. van der Vliet, A. P. Paulikas, V. R. Stamenkovic, N. M. Markovic, *Nat. Chem.* **2013**, *5*, 300.
[23] J. Zheng, W. Sheng, Z. Zhuang, B. Xu, Y. Yan, *Sci. Adv.* **2016**, *2*, 1501602.
[24] S. Lu, J. Pan, A. Huang, L. Zhuang, J. Lu, *Proc. Natl. Acad. Sci. USA* **2008**, *105*, 20611.
[25] F. Yang, X. Bao, Y. Zhao, X. Wang, G. Cheng, W. Luo, *J. Mater. Chem. A* **2019**, *7*, 10936.
[26] A. Roy, M. R. Talarposhti, S. J. Normile, I. V Zenyuk, V. De Andrade, K. Artyushkova, A. Serov, P. Atanassov, *Sustainable Energy Fuels* **2018**, *2*, 2268.
[27] S. Kabir, K. Lemire, K. Artyushkova, A. Roy, M. Odgaard, D. Schlueter, A. Oshchepkov, A. Bonnefont, E. Savinova, D. C. Sabarirajan, P. Mandal, E. J. Crumlin, I. V. Zenyuk, P. Atanassov, A. Serov, *J. Mater. Chem. A* **2017**, *5*, 24433.
[28] Z. Zhuang, S. A. Giles, J. Zheng, G. R. Jenness, S. Caratzoulas, D. G. Vlachos, Y. Yan, *Nat. Commun.* **2016**, *7*, 10141.
[29] A. G. Oshchepkov, A. Bonnefont, S. N. Pronkin, O. V Cherstiouk, C. Ulhaq-Bouillet, V. Papaefthimiou, V. N. Parmon, E. R. Savinova, *J. Power Sources* **2018**, *402*, 447.
[30] E. S. Davydova, F. D. Speck, M. T. Y. Paul, D. R. Dekel, S. Cherevko, *ACS Catal.* **2019**, *9*, 6837.
[31] E. Davydova, J. Zaffran, K. Dhaka, M. Toroker, D. Dekel, *Catalysts* **2018**, *8*, 454.
[32] M. Alesker, M. Page, M. Shviro, Y. Paska, G. Gershinsky, D. R. Dekel, D. Zitoun, *J. Power Sources* **2016**, *304*, 332.
[33] I. Bakos, A. Paszternák, D. Zitoun, *Electrochim. Acta* **2015**, *176*, 1074.
[34] H. A. Miller, A. Lavacchi, F. Vizza, M. Marelli, F. Di Benedetto, F. D'Acapito, Y. Paska, M. Page, D. R. Dekel, *Angew. Chem., Int. Ed.* **2016**, *55*, 6004.
[35] H. A. Miller, F. Vizza, M. Marelli, A. Zadick, L. Dubau, M. Chatenet, S. Geiger, S. Cherevko, H. Doan, R. K. Pavlicek, S. Mukerjee, D. R. Dekel, *Nano Energy* **2017**, *33*, 293.
[36] H. Yu, E. S. Davydova, U. Ash, H. A. Miller, L. Bonville, D. R. Dekel, R. Maric, *Nano Energy* **2019**, *57*, 820.
[37] M. Bellini, M. V. Pagliaro, A. Lenarda, P. Fornasiero, M. Marelli, C. Evangelisti, M. Innocenti, Q. Jia, S. Mukerjee, J. Jankovic, L. Wang, J. R. Varcoe, C. B. Krishnamurthy, I. Grinberg, E. Davydova, D. R. Dekel, H. A. Miller, F. Vizza, *ACS Appl. Energy Mater.* **2019**, *2*, 4999.
[38] N. Ralbag, E. S. Davydova, M. Mann-Lahav, P. Cong, J. He, A. M. Beale, G. S. Grader, D. Avnir, D. R. Dekel, *J. Electrochem. Soc.* **2020**, *167*, 054514.
[39] V. Yarmiayev, M. Alesker, A. Muzikansky, M. Zysler, D. Zitoun, *J. Electrochem. Soc.* **2019**, *166*, F3234.
[40] Z. A. Feng, F. El Gabaly, X. Ye, Z.-X. Shen, W. C. Chueh, *Nat. Commun.* **2014**, *5*, 4374.
[41] K. P. Kepp, *Inorg. Chem.* **2016**, *55*, 9461.
[42] K. R. Priolkar, P. Bera, P. R. Sarode, M. S. Hegde, S. Emura, R. Kumashiro, N. P. Lalla, *Chem. Mater.* **2002**, *14*, 2120.
[43] A. Primavera, A. Trovarelli, C. de Leitenburg, G. Dolcetti, J. Llorca, *Stud. Surf. Sci. Catal* **1998**, *119*, 87.
[44] L. Meng, J.-J. Lin, Z.-Y. Pu, L.-F. Luo, A.-P. Jia, W.-X. Huang, M.-F. Luo, J.-Q. Lu, *Appl. Catal., B* **2012**, *119*, 117.
[45] R. V Gulyaev, T. Y. Kardash, S. E. Malykhin, O. A. Stonkus, A. S. Ivanova, A. I. Boronin, *Phys. Chem. Chem. Phys.* **2014**, *16*, 13523.
[46] D. O. Scanlon, B. J. Morgan, G. W. Watson, *Phys. Chem. Chem. Phys.* **2011**, *13*, 4279.
[47] H. Tan, J. Wang, S. Yu, K. Zhou, *Environ. Sci. Technol.* **2015**, *49*, 8675.
[48] M. Cargnello, N. L. Wieder, T. Montini, R. J. Gorte, P. Fornasiero, *J. Am. Chem. Soc.* **2010**, *132*, 1402.
[49] C. M. Sims, R. A. Maier, A. C. Johnston-Peck, J. M. Gorham, V. A. Hackley, B. C. Nelson, *Nanotechnology* **2019**, *30*, 085703.
[50] P. H. Ho, M. Ambrosetti, G. Groppi, E. Tronconi, J. Jaroszewicz, F. Ospitali, E. Rodríguez-Castellón, G. Fornasari, A. Vaccari, P. Benito, *Catal. Sci. Technol.* **2018**, *8*, 4678.
[51] Z. Yang, Z. Lu, G. Luo, K. Hermansson, *Phys. Lett. A* **2007**, *369*, 132.
[52] Y. Ma, Q. Ge, W. Li, H. Xu, *Appl. Catal., B* **2009**, *90*, 99.
[53] A. Devadas, S. Vasudevan, F. Epron, *J. Hazard. Mater.* **2011**, *185*, 1412.
[54] Y. Wang, G. Wang, G. Li, B. Huang, J. Pan, Q. Liu, J. Han, L. Xiao, J. Lu, L. Zhuang, *Energy Environ. Sci.* **2015**, *8*, 177.
[55] S. Lu, Z. Zhuang, *J. Am. Chem. Soc.* **2017**, *139*, 5156.
[56] X. Qin, L. Zhang, G.-L. Xu, S. Zhu, Q. Wang, M. Gu, X. Zhang, C. Sun, P. B. Balbuena, K. Amine, M. Shao, *ACS Catal.* **2019**, *9*, 9614.
[57] S. H. Hakim, C. Sener, A. C. Alba-Rubio, T. M. Gostanian, B. J. O'Neill, F. H. Ribeiro, J. T. Miller, J. A. Dumesic, *J. Catal.* **2015**, *328*, 75.
[58] C. Sener, T. S. Wesley, A. C. Alba-Rubio, M. D. Kumbhalkar, S. H. Hakim, F. H. Ribeiro, J. T. Miller, J. A. Dumesic, *ACS Catal.* **2016**, *6*, 1334.
[59] A. C. Alba-Rubio, C. Sener, S. H. Hakim, T. M. Gostanian, J. A. Dumesic, *ChemCatChem* **2015**, *7*, 3881.
[60] R. Carrasquillo-Flores, I. Ro, M. D. Kumbhalkar, S. Burt, C. A. Carrero, A. C. Alba-Rubio, J. T. Miller, I. Hermans, G. W. Huber, J. A. Dumesic, *J. Am. Chem. Soc.* **2015**, *137*, 10317.
[61] I. Ro, Y. Liu, M. R. Ball, D. H. K. Jackson, J. P. Chada, C. Sener, T. F. Kuech, R. J. Madon, G. W. Huber, J. A. Dumesic, *ACS Catal.* **2016**, *6*, 7040.
[62] R. K. Singh, R. Rahul, M. Neergat, *Phys. Chem. Chem. Phys.* **2013**, *15*, 13044.
[63] K. Lee, O. Savadogo, A. Ishihara, S. Mitsushima, N. Kamiya, K. Ota, *J. Electrochem. Soc.* **2006**, *153*, A20.
[64] S. Deshpande, S. Patil, S. V. N. T. Kuchibhatla, S. Seal, *Appl. Phys. Lett.* **2005**, *87*, 133113.
[65] J. Ma, Y. Lou, Y. Cai, Z. Zhao, L. Wang, W. Zhan, Y. Guo, Y. Guo, *Catal. Sci. Technol.* **2018**, *8*, 2567.
[66] R. K. Singh, R. Ramesh, R. Devivaraprasad, A. Chakraborty, M. Neergat, *Electrochim. Acta* **2016**, *194*, 199.
[67] M. Lukaszewski, M. Soszko, A. Czerwiński, *Int. J. Electrochem. Sci.* **2016**, *11*, 4442.
[68] T. J. Omasta, X. Peng, H. A. Miller, F. Vizza, L. Wang, J. R. Varcoe, D. R. Dekel, W. E. Mustain, *J. Electrochem. Soc.* **2018**, *165*, J3039.
[69] Y. Cong, I. T. McCrum, X. Gao, Y. Lv, S. Miao, Z. Shao, B. Yi, H. Yu, M. J. Janik, Y. Song, *J. Mater. Chem. A* **2019**, *7*, 3161.
[70] I. B. Aragao, I. Ro, Y. Liu, M. Ball, G. W. Huber, D. Zanchet, J. A. Dumesic, *Appl. Catal., B* **2018**, *222*, 182.
[71] I. Ro, I. B. Aragao, Z. J. Brentzel, Y. Liu, K. R. Rivera-Dones, M. R. Ball, D. Zanchet, G. W. Huber, J. A. Dumesic, *Appl. Catal., B* **2018**, *231*, 182.
[72] M. R. Ball, K. R. Rivera-Dones, E. Stangland, M. Mavrikakis, J. A. Dumesic, *J. Catal.* **2019**, *370*, 241.
[73] I. Ro, R. Carrasquillo-Flores, J. A. Dumesic, G. W. Huber, *Appl. Catal., A* **2016**, *521*, 182.
[74] I. Ro, C. Sener, T. M. Stadelman, M. R. Ball, J. M. Venegas, S. P. Burt, I. Hermans, J. A. Dumesic, G. W. Huber, *J. Catal.* **2016**, *344*, 784.
[75] Y. Liu, F. Göeltl, I. Ro, M. R. Ball, C. Sener, I. B. Aragão, D. Zanchet, G. W. Huber, M. Mavrikakis, J. A. Dumesic, *ACS Catal.* **2017**, *7*, 4550.
[76] M. R. Ball, T. S. Wesley, K. R. Rivera-Dones, G. W. Huber, J. A. Dumesic, *Green Chem.* **2018**, *20*, 4695.
[77] I. Ro, I. B. Aragao, J. P. Chada, Y. Liu, K. R. Rivera-Dones, M. R. Ball, D. Zanchet, J. A. Dumesic, G. W. Huber, *J. Catal.* **2018**, *358*, 19.
[78] R. Bock, I. L. Marr, *A Handbook of Decomposition Methods in Analytical Chemistry*, Wiley, New York **1979**.
[79] E. S. Analysis, *Society* **2000**, *12*, 1.
[80] A. N. Correia, L. H. Mascaro, S. A. S. Machado, L. A. Avaca, *Electrochim. Acta* **1997**, *42*, 493.

[81] L. L. Fang, Q. Tao, M. F. Li, L. W. Liao, D. Chen, Y. X. Chen, *Chin. J. Chem. Phys.* **2010**, *23*, 543.
[82] A. Zadick, L. Dubau, N. Sergent, G. Berthomé, M. Chatenet, *ACS Catal.* **2015**, *5*, 4819.
[83] J. Zheng, Y. Yan, B. Xu, *J. Electrochem. Soc.* **2015**, *162*, F1470.
[84] W. Sheng, Z. Zhuang, M. Gao, J. Zheng, J. G. Chen, Y. Yan, *Nat. Commun.* **2015**, *6*, 5848.
[85] L. Wang, E. Magliocca, E. L. Cunningham, W. E. Mustain, S. D. Poynton, R. Escudero-Cid, M. M. Nasef, J. Ponce-González, R. Bance-Souahli, R. C. T. Slade, D. K. Whelligan, J. R. Varcoe, *Green Chem.* **2017**, *19*, 831.
[86] J. Ponce-González, D. K. Whelligan, L. Wang, R. Bance-Soualhi, Y. Wang, Y. Peng, H. Peng, D. C. Apperley, H. N. Sarode, T. P. Pandey, A. G. Divekar, S. Seifert, A. M. Herring, L. Zhuang, J. R. Varcoe, *Energy Environ. Sci.* **2016**, *9*, 3724.
[87] T. N. Danks, R. C. T. Slade, J. R. Varcoe, *J. Mater. Chem.* **2003**, *13*, 712.
[88] J. R. Varcoe, R. C. T. Slade, E. Lam How Yee, S. D. Poynton, D. J. Driscoll, D. C. Apperley, *Chem. Mater.* **2007**, *19*, 2686.